Intrinsic and extrinsic size effects on deformation in nanolayered Cu/Zr micropillars: From bulk-like to small-volume materials behavior

J.Y. Zhang [a], S. Lei [a], J. Niu [a], Y. Liu [b], G. Liu [a,*], X. Zhang [b,*], J. Sun [a,*]

[a] *State Key Laboratory for Mechanical Behavior of Materials, Xi'an Jiaotong University, Xi'an 710049, People's Republic of China*
[b] *Department of Mechanical Engineering, Mater. Sci. Eng. Program, Texas A&M University, College Station, TX 77843-3123, USA*

Abstract

By using microcompression methodology, deformation of nanolayered Cu/Zr micropillars was systematically investigated within wide ranges of intrinsic layer thickness (5–100 nm) and extrinsic sample size (300–1200 nm). The intrinsic size effect, extrinsic size effect and their interplay were respectively revealed. Competition between the intrinsic and extrinsic size effects leads to experimental observation of a critical layer thickness of ∼20 nm, above which the deformation is predominantly intrinsic-size-related and insensitive to sample size, while below which the two size effects are comparable. The underlying deformation mechanisms were proposed to transform from bulk-like to small-volume materials behavior. Deformation mode is correspondingly transited from homogeneous extrusion/barreling to inhomogeneous shear banding, but the two competing modes coexist in the layer thickness range from ∼50 to 20 nm. In the regime of shear deformation, the extrinsic size dependence is displayed in that the deformation was controlled by shear bands nucleation in larger pillars while controlled by shear bands propagation in smaller pillars. A deformation mode map is developed to clearly elucidate the coupling intrinsic and extrinsic size effects on the deformation mode of nanolayered pillars.
© 2012 Acta Materialia Inc. Published by Elsevier Ltd. All rights reserved.

Keywords: Nanolayered micropillar; Deformation; Dislocation source; Size effect

1. Introduction

The sample-size-independent crystalline strength in bulk (microcrystal) metals is proportional to the increasing-with-strain dislocation density (ρ) via the Taylor relation: $\sigma \propto b\mu\sqrt{\rho}$ [1], whereby dislocations multiply via double-cross slip and by operation of pinned or Frank–Read (F–R) type dislocation sources [2], due to the extrinsic size far larger than their largest intrinsic size. In contrast, in small-scaled materials such as nanolaminates and micro- or nanopillars, these two quantities generally overlap so that the deformation related physical mechanism can begin to "feel" the presence of the surface/interface, rendering the so-called size effect [3–5].

For example, recent experiments involving compression of small-scaled pillars with unusual mechanical characteristics [6–10] have shown that the extrinsic size-dependent yield stress differs fundamentally between face-centered-cubic (fcc), hexagonal close packed (hcp) and body-centered-cubic (bcc) single crystals with non-zero initial dislocation density. In all the three types of non-pristine crystals, plasticity at small length scale is truly a function of microstructure [11], which in turn defines size effect, i.e. the yield strength σ_y scales inversely with some power of the pillar diameter ϕ: in fcc pillars the relationship is $\sigma_y \propto \phi^{-(0.61\sim0.97)}$ [3,5,12,13], whereas hcp pillars exhibit a less pronounced size effect (for dislocation slip) with $\sigma_y \propto \phi^{-(0.44\sim0.64)}$ [5,14,15], followed by bcc pillars ($\sigma_y \propto \phi^{-(0.22\sim0.48)}$) [5,9,16–18]. Further studies showed that their σ_y can also be influenced by the aspect ratio (β, the ratio of pillar height to diameter), i.e. larger β equates to lower strength [19,20]. Currently, the micro-mechanisms

---

* Corresponding authors. Tel.: +86 2982668695; fax: +86 2982663453.
  E-mail addresses: lgsammer@mail.xjtu.edu.cn (G. Liu), zhangx@ta-mu.edu (X. Zhang), junsun@mail.xjtu.edu.cn (J. Sun).

of size-dependent strengthening for single crystal pillars are commonly explained by dislocation starvation [21–23] and source truncation [24–26] or source exhaustion [27–29] effects. Although the precise nature of either type of source is being vigorously pursued, a general agreement exists that nanosized pillars are starved of mobile dislocations and therefore the nucleation of surface dislocations is required to accommodate the induced plastic deformation [21–23,30–32]. In contrast, for micron- and submicron-sized pillars the multiplication of dislocations by the activation of internal dislocation sources is the dominant mechanism for plastic flow [24–26,30–32]. As the strain is increased the rising dislocation density in these pillars leads to dislocation reactions that shut off the weak sources, creating "exhaustion hardening" [23,27,28]. Further advances investigating in depth the crystalline plasticity in the sub-micron regime ($100 < \phi < 200$ nm) have revealed that both the truncation of spiral dislocation sources (in fcc pillar)/self-multiplication (in bcc pillar) and exhaustion of defects available within the specimen, contribute to high strengths and related size-effects in small volumes and should be considered simultaneously rather than exclusively [30,32–36]. In order to differentiate these mechanisms, an effective approach to an answer that "averages over" the results of many events rather than one based on the results of a few observations is to examine the strength variation at a fixed sample size and to use these results to ascertain the location of the operative dislocation source [20,37]. The nanolayered micropillars thus can be chosen as an ideal vehicle to prove this idea, due to their unique microstructures (e.g. abundance of interfaces and uniformed grain size).

On the other hand, nanostructured metallic multilayers represent a new class of engineering materials and provide ideal systems for the exploration of length-scale-dependent plasticity [38–45]. Generally, the hardness/strength of multilayers (e.g. Cu/Nb [38,46], Cu/Cr [47,48], Cu/Ni [49] and Cu/Zr [38]) monotonically increases with decreasing layer thickness (h) down to ~2–5 nm, as is consistent with the creed of "smaller is stronger". As their intrinsic size h shrinking towards to nanoscale, related strengthening mechanisms such as the Hall–Petch (H–P) model based on dislocation pile-ups [50], confined layer slip (CLS) model involving single dislocation loops glide in isolated layers [51,52] and interface barrier strength (IBS) model considering dislocation cutting cross the interface [53,54] have been the subject of extensive studies. The question arises: during plastic deformation of these nanolayered materials, where do the dislocations originate from (bulk sources or surface/interface sources)? It is also worthy to question how the deformation mechanism influences the mechanical response of nanostructured multilayers. Unlike the traditional nanoindentation test causing a non-uniform stress state in the plastic zone within the sample [39,55], the microcompression methodology [7] opened new avenues for studying their deformation and strain hardening/softening behavior of multilayers in a nominally homogeneous stress state [40,41,44,45,56–58,43].

Since interface of multilayers itself is a defect, it is natural to ask to what degree the strength of such interface-confined materials reflect interface properties and interface-mediated processes. Recently, Mara et al. [44,45] pointed out that no extrinsic size effects are observed in uniaxially compressed Cu/Nb micropillars with equal h of 5 and 40 nm and much larger ϕ between 4 and 8 μm. A conjecture thus is made that the strength is fully controlled by the intrinsic size h, whereby individual dislocations transmit through the Cu/Nb interfaces, rather than by the extrinsic size ϕ [44,45]. In previous works, we also reported preliminary results of intrinsic size-controlled uniform to shear deformation transition and strain hardening–softening behaviors in nanolayered Cu/Zr pillars [57,58]. But the underlying deformation mechanisms were unknown and the extrinsic size effect was not carefully examined. In the present study, we perform systematic investigations into the mechanical response and deformation mode of nanolayered Cu/Zr pillars within wide ranges of intrinsic layer thickness (h from 100 down to 5 nm) and extrinsic sample size (ϕ from 1200 to 300 nm). Specifically, the deformation mechanisms were proposed to transit from the bulk-like behavior at $h > {\sim}20$ nm to small-volume material behavior at $h < {\sim}20$ nm, based on the semi-quantitative analyses of dynamic behaviors of dislocations. We present a clear demonstration of the roles played by the microstructural constraints (h) and dimensional constraints (ϕ) of such small-scaled samples in dislocation nucleation to deeply understand the interplay of the two reduced scales: h vs. ϕ. Also we show in the case of nanolayered micropillars, for which there is a fixed extrinsic/intrinsic size set by the pillar diameter/layer thickness, that "smaller is stronger" still holds true.

2. Experimental procedures

Nanostructured Cu/Zr multilayers were deposited on a Si (100) substrate by direct current (DC) magnetron sputtering at room temperature. The constituents within the Cu/Zr multilayers have equal individual layer thickness, h, varying from 5 to 100 nm. The total thickness of the Cu/Zr multilayers was ~1.6 μm. X-ray diffraction (XRD) experiments were performed in a Bruker D8 Discover X-ray powder diffractometer. High resolution transmission electron microscopy (HRTEM) observations and energy dispersive X-ray (EDX) analyses were performed to observe the modulation structure and the interface structure. More details can be found in our previous result [57].

Then the focused ion beam (FIB)-machined nanolayered micropillars with ϕ spanning from ~300 to 1200 nm fabricated from Cu/Zr multilayers were uniaxially compressed in a Hystron Ti 950 with a 10 μm side-flat quadrilateral cross-section diamond indenter at loading rate ~0.35 nm s^{-1} (corresponding to a constant strain rate of 2×10^{-4} s^{-1}) up to 15–30% strain. (More information about the fabrication of Cu/Zr pillars can be found in Ref. [57].) Force–displacement data were continuously

recorded, and the initial geometry of the pillar was measured from the scanning electron microscopy (SEM) images. The cross-sectional area at half height of the pillar (A_0) and the initial height (L_0) were used for calculations. Following our previous work [57], an attempt was made to correct for the compliance of the base of the pillar by using the model of a perfectly rigid circular flat punch being indented onto an isotropic half space first proposed by Sneddon [59]. After obtaining the true compliance of the pillar, the "corrected" load–displacement curves were obtained, then the engineering stress–strain curves were converted into true stress–strain curves by using the homogeneous deformation model (assume no volume change during the deformation [6,39,60] and the final height and average cross-sectional area are L_p and A_p, respectively, such that $L_0A_0 = L_pA_p$). Then the true strain ε_T and true stress σ_T can be expressed as [57]:

$$\varepsilon_T = \frac{1}{E}\frac{PL_p}{A_0L_0} + \ln\left(\frac{L_0}{L_p}\right) \tag{1}$$

and

$$\sigma_T = \frac{P}{A_p} = \frac{PL_p}{A_0L_0} = \frac{P}{A_0L_0}\left\{L_0 - \left[u_{tot} - \frac{\pi P(1 - v_m^2)}{2E\sqrt{A_p}}\right]\right\} \tag{2}$$

where P is the load, E is the modulus of the Cu/Zr multilayers calculated from the rule-of-mixtures, u_{tot} is the total displacement, and v_m is the Poisson's ratio of the multilayers ($\sim$0.33). It should be pointed out that the deformation under 10% strain could be simply regarded as homogeneous, because the softening was experimentally found to occur after $\sim$10% strain in present nanolayered pillars (see the text below), as is consistent with other results (e.g. Al/Al3Sc [39] and Al/TiN [43]). The work hardening parameter derived from the above true stress–strain curves could be approximately used to investigate both intrinsic and extrinsic size effect on the deformation behaviors of nanolayered pillars. For comparison reasons, the nanocrystalline Zr and Cu pillars with $\phi = 300$–1200 nm were respectively fabricated from the 1.6 μm thick monolithic Zr and Cu thin films and then tested following the same treatment. The strength (σ) at plastic strain $\varepsilon_p = 0.2\%$ ($\sigma_{0.2\%}$), at $\varepsilon_p = 2\%$ ($\sigma_{2\%}$) and the maximum strength at $\varepsilon_p \sim 5\%$ (σ_{max}) were obtained from the true stress–strain curves.

3. Results

3.1. Microstructure of Cu/Zr multilayers

XRD results revealed that all Cu/Zr multilayers with opaque incoherent interface have polycrystalline structure with (1 1 1) texture in Cu layers and with (0 0 0 2) texture in Zr layers. Cross-sectional views of the Cu/Zr multilayers from TEM observations are displayed in Fig. 1, showing columnar grains in the Cu layers and ultra-fine nanocrystals in the Zr layers. The average grain sizes of Cu and Zr scale with their layer thickness, respectively. No significant intermixing between Cu and Zr has been observed as proved by the interface HRTEM (see Fig. 1a and d). Some planar defects such as growth twins and intrinsic stacking faults (ISFs) are observed in the Cu layers, as shown in Fig. 1b, d and e, respectively. The average grain sizes of monolithic Cu and Zr films are $\sim$160 and $\sim$30 nm, respectively.
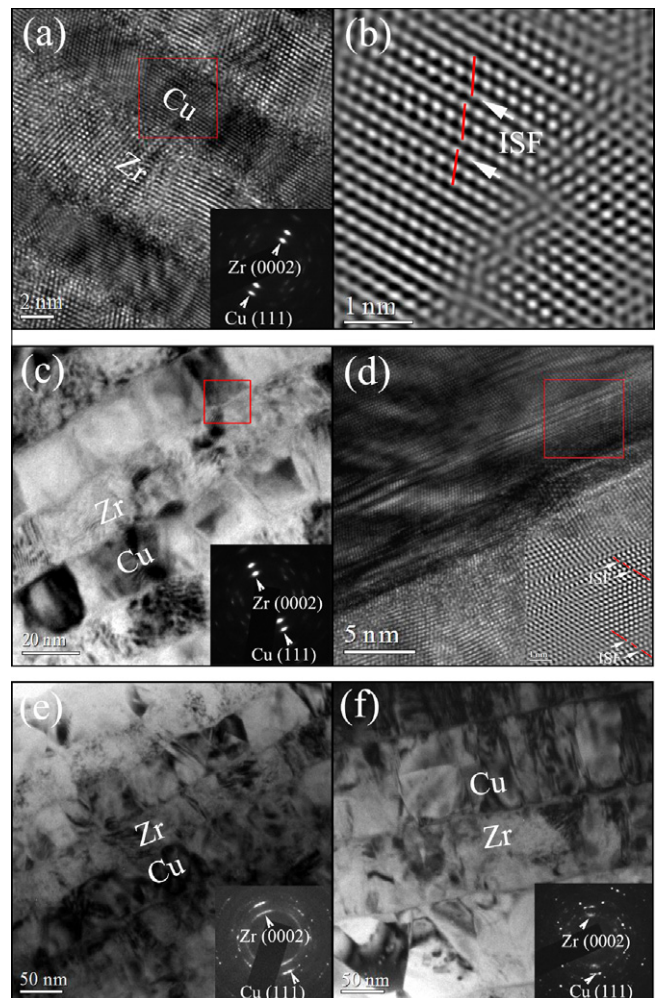

Fig. 1. Bright-field cross-sectional TEM micrograph showing the microstructure of the (a) $h = 5$ nm, (c) $h = 20$ nm, (e) $h = 50$ nm and (f) $h = 100$ nm Cu/Zr multilayers. Inset is the corresponding selected area diffraction patterns (SADP); (b) is the inverse fast Fourier transform (IFFT) HRTEM image of white squared box region in (a), showing intrinsic stacking fault (ISF) in Cu; (d) is the HRTEM images typically showing the Cu/Zr interface of the red square boxed area in (c). Inset is the inverse fast Fourier transform (IFFT) HRTEM image of red squared box region in (d), showing ISF in Cu.

3.2. Mechanical response of Cu/Zr micropillars

Fig. 2a and b shows the typical true stress–strain curves of $\phi = 600$ nm and $h = 10$ nm Cu/Zr pillars, respectively. As shown in Fig. 2a and b, there clearly exist size dependences in the deformation behavior, with the smaller h or ϕ pillars having the higher flow stresses. All the pillars show three regimes in the true stress–strain curves. In
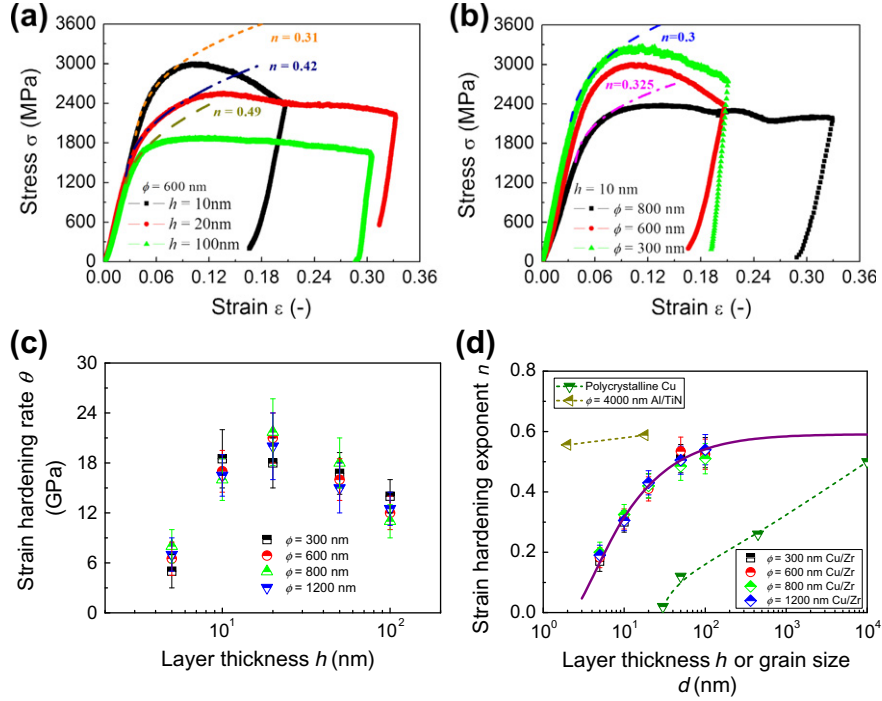
Fig. 2. (a) True stress–strain plots for the $\phi = 600$ nm Cu/Zr micropillars with three different h, and (b) true stress–strain plot for $h = 10$ nm Cu/Zr micropillars with various ϕ loaded perpendicular to the layer interface. The strain hardening regime (regime II) is fitted by using power-law strain hardening equation: $\sigma \propto \varepsilon_p^n$. (c) The strain hardening rate θ of Cu/Zr micropillars with four different ϕ as a function of h. (d) The strain hardening exponent n as a function of h, compared with that of Cu [61,65] (as a function of grain size d) and nanolayered Al/TiN [43] (as a function of h).

regime I, the curves show a linear elastic behavior until the first yield point (σ_0) is reached ($\varepsilon = 0.02$–0.04). Regime II shows a strain hardening behavior at a strain level of ~ 0.05–0.1, which can be described by the power-law strain hardening equation, i.e. Ludwik's equation [43,57,61], by simply assuming this equation still operative in the small-scale regime:

$$\sigma = K_1 + K_2 \varepsilon_p^n \qquad (3)$$

where K_1 represents the initial yield stress, K_2 is the strengthening coefficient (i.e. the strength increment due to strain hardening at plastic strain $\varepsilon_p = 1$), and n is the strain hardening exponent. By using Eq. (3) and taking $K_1 = \sigma_0$, we fitted the true stress–strain curves in regime II, as shown in Fig. 2a and b. The strain hardening rate θ at this regime can be estimated by using the following equation [43,57]:

$$\theta = \frac{d\sigma}{d\varepsilon} = \frac{n(\sigma_{2\%} - \sigma_{0.2\%})}{(\varepsilon_{2\%} - \varepsilon_{0.2\%})} \qquad (4)$$

From Fig. 2c and d, one can clearly see that both the strain hardening rate (θ) and strain hardening exponent (n) obtained from regime II are intrinsic rather than extrinsic size-controlled. A maximum $\theta \sim 20$ GPa is observed at $h = 20$ nm at $\varepsilon_p = 2\%$, while n monotonically decreases from ~ 0.5 down to ~ 0.2 as reducing h from 100 to 5 nm. In regime III, at strains greater than ~ 0.1, strain softening is also observed from the true stress–strain curves. As is evident in the true stress–strain plots, there is a decrease in strain softening as the h or ϕ increases.

The intrinsic and extrinsic size effects on strength of the Cu/Zr pillars are studied in comparison. In Fig. 3a and b, $\sigma_{0.2\%}$ is depicted as a function of ϕ and h, respectively. From Fig. 3a for the Cu/Zr pillars with constant h, one can see that the $\sigma_{0.2\%}$ presents weak dependence of ϕ when $h > 20$ nm, while $\sigma_{0.2\%}$ strongly depends on ϕ when $h < 20$ nm. It is suggested that the extrinsic size effect is remarkable only at small h. By contrast, $\sigma_{0.2\%}$ rises significantly as h decreases from 100 to 5 nm (see Fig. 3b for the Cu/Zr pillars with constant ϕ or β). This means that the intrinsic size effect on strength of Cu/Zr pillars is notable within the whole range studied.

It is generally accepted that deformation from motion of dislocations produced via activation of the pinned bulk sources usually needs lower external stress than that of via dislocation nucleation from the surface/interface. To distinguish the dislocation nucleation mechanisms (characterized by different stress levels), the strengths $\sigma_{2\%}$ and σ_{max} were also plotted against ϕ and h, as shown in Fig. 3c and d (for $\sigma_{2\%}$) and (e) and (f) (for σ_{max}) respectively. They exhibit size-dependent trends similar to those of $\sigma_{0.2\%}$. In addition, the Zr pillars also exhibit strong extrinsic size effect, which monotonically increase with reducing ϕ (Cu pillars behave the same way).

3.3. Deformation behavior of Cu/Zr micropillars

Fig. 4a–h shows the SEM images taken after the uniaxial compression of the pillars with $h = 100$ nm (a, b), $h = 50$ nm (c, d), $h = 20$ nm (e, f) and $h = 10$ nm (g, h). It
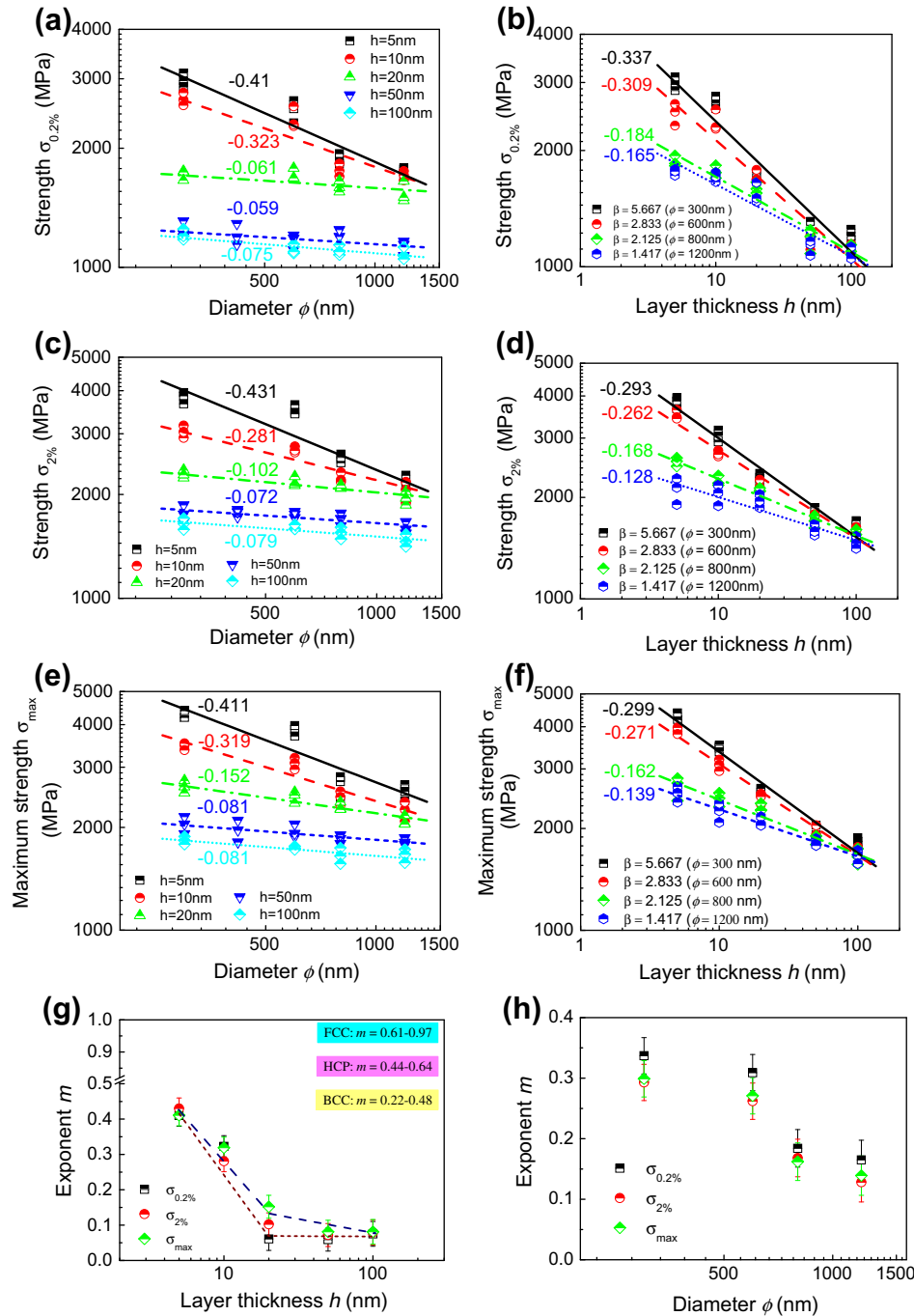
Fig. 3. The strengths of $\sigma_{0.2\%}$ (a, b), $\sigma_{2\%}$ (c, d) and σ_{max} (e, f) as a function of ϕ and h, respectively. The strength scaling exponent m as a function of h (g) and ϕ (h), respectively.

is seen that the deformed $h = 100$ nm pillar shows plastic barreling and extrusion of soft Cu layers. In contrast, the deformed $h = 20$ and 10 nm pillars display shear deformation across the compression plane without significant extrusion. In the intermediate $h = 50$ nm pillars, both barreling (accompanied with extrusion) and shearing are observed. The h-dependent transition of deformation mode is similar to that of rolled Cu/Nb nanolaminates [62] and compressed Al/Pd micropillars [56]. Furthermore, accord-

ing to the SEM/FIB micrographs it is interesting to note that as ϕ decreases from 1200 to 600 nm (or β increases from 1.4 to 2.8), the apparent deformation mode shows a gradual transition from highly inhomogeneous shear deformation to relatively homogeneous shear failure at the shearing regime of $h < 50$ nm. The well-developed major shear band with sharp leading fronts at large ϕ (or small β) is gradually changed to localized shear deformation with rounded leading fronts at the upper part of the pillars. This
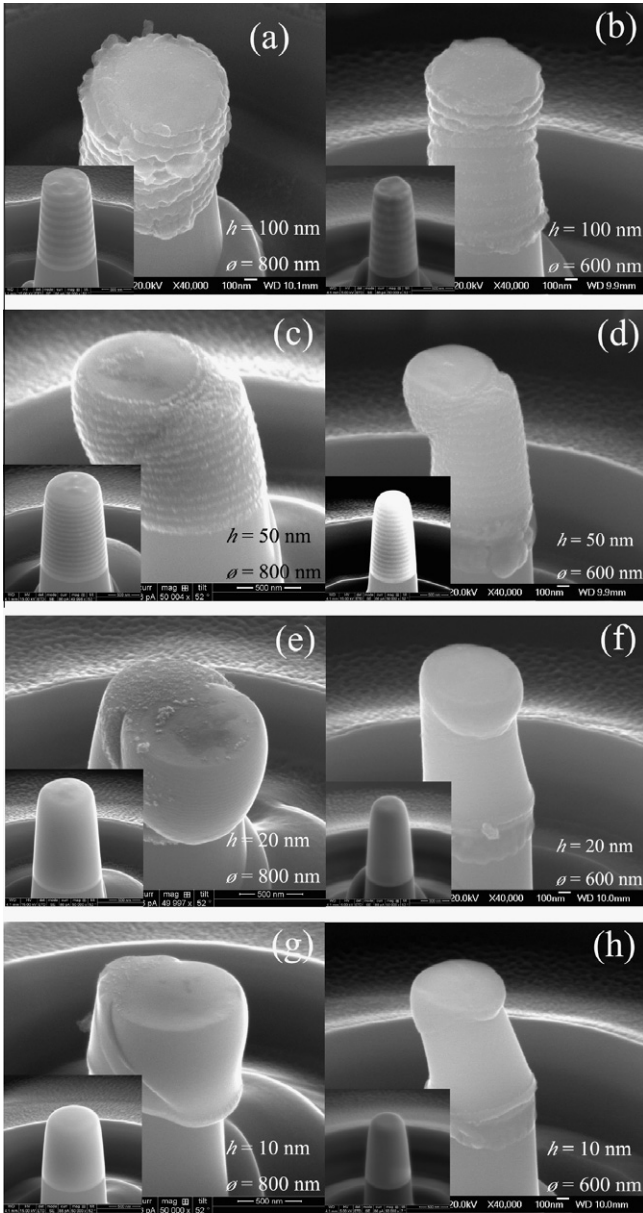
Fig. 4. Typical SEM images of nanolayered Cu/Zr micropillars with four different h after the uniaxial compression tests. (a) $\phi = 800$ nm and (b) $\phi = 600$ nm micropillar with $h = 100$ nm after compression showing barreling of the micropillar and extrusion from individual Cu layers; (c) $\phi = 800$ nm and (d) $\phi = 600$ nm micropillar with $h = 50$ nm after compression showing squeezing and shearing of the pillar; and (e) $\phi = 800$ nm and (f) $\phi = 600$ nm micropillar with $h = 20$ nm, and (g) $\phi = 800$ nm and (h) $\emptyset = 600$ nm micropillar with $h = 10$ nm after compression showing shearing the micropillar. Inset is the corresponding SEM images of the as-milled pillar.

phenomenon becomes more significant with further reducing ϕ to 300 nm (or increasing β to 5.7). However, when fixing $\beta = 5.7$, the $h = 50$ nm Cu/Zr pillars show plastic barreling and extrusion (the $\beta = 1.4$ pillar behaves the same way), while the $h = 20$ nm Cu/Zr pillars exhibit extrusion + shearing deformation (see Fig. 5a and b, respectively). This indicates that the deformation mode of nanolayered pillars can be influenced by both h and ϕ.
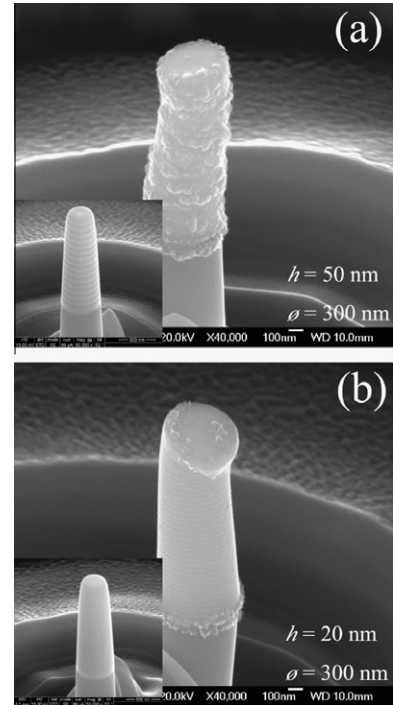

Fig. 5. Typical SEM images of $\phi = 300$ nm nanolayered Cu/Zr micropillars (a) $h = 50$ nm micropillar showing barreling of the micropillar and extrusion from individual Cu layers and (b) $h = 20$ nm micropillar showing squeezing and shearing of the pillar. Inset shows the corresponding SEM images of the as-milled pillar.

4. Discussion

4.1. Hardening behavior of nanolayered micropillars

4.1.1. Intrinsic size-controlled hardening capability

Both θ and n are important parameters reflecting a metallic material's hardening property, which are closely linked to the stored dislocation density (ρ) [58,63,64]. The extrinsic size ϕ-independent extraordinary θ in Fig. 2c much higher than that of bulk metals (maximum θ ~2.5 GPa for Cu [1]) with an inverse h-effect is caused by more glide–interface dislocations interactions, leading to increasing θ with reducing h to ~20 nm, below which the dislocation cross-slip lower θ [57]. This was physically and quantitatively explained in terms of reduced dislocations storage rates [58].

The present results also exhibited that n was determined by intrinsic rather than extrinsic size, and that n continuously decreased with reducing h, analogues to that of polycrystalline Cu [61,65] and Al/TiN [43] pillars (see Fig. 2d). It is suggested that the uniform deformability of multilayers monotonically decreases with reducing h [66,67], as demonstrated from the SEM observations (see Fig. 4). In our previous work [58], we have found that an inversely linear relationship between n and strength of Cu/Zr pillars, i.e. $n \propto k\sigma_{CLS}$, where k is a fitting parameter, σ_{CLS} is the pillar strength and can be written as [38,46,57]:

$$\sigma_{\text{CLS}} = \frac{\mu^* b \sin\varphi}{8\pi sh} \left(\frac{4-v}{1-v}\right) \ln\left(\frac{\alpha h}{b \sin\varphi}\right) + \frac{\mu^* b}{\lambda(1-v)} - \frac{f}{h} \quad (5)$$

where s is the Schmid factor; φ is the angle between the slip plane and the interface; b is the magnitude of the Burgers vector; v is the Poisson ratio for Cu; λ is the mean spacing of glide loops in a parallel array, inversely proportional to the square root of the total dislocation density ρ; $\mu^* = (\mu_{\text{Zr}} \cdot \mu_{\text{Cu}})/(V_{\text{Zr}} \cdot \mu_{\text{Cu}} + V_{\text{Cu}} \cdot \mu_{\text{Zr}})$ is the effective shear modulus of Cu/Zr multilayers which can be estimated by the shear modulus μ_{Cu} and volume fraction V_{Cu} of the Cu layer and those of the Zr layer; geometrical factor α is the dislocation core spreading factor, varying from 0 (for a compact core) to 1 (for a spread core) and contains the contribution of extrinsic size constraint effect on strength [15,19,68]; and f is the characteristic interface stress of the multilayer, typically $f = 2$–3 J m^{-2} [46]. With a series of parameters of $s = 0.33$, $\mu^* = 40.6$ GPa, $b = 0.2556$ nm, $\alpha = 0.55$, $v = 0.343$, $\varphi = 70.5°$, $\lambda = 10$ nm [69] and Eq. (5), the dependence of n on h is quantitatively calculated and shown in Fig. 2d as the solid curve, consisting well with the measured n with $k = -1.5 \times 10^{-4}$ MPa. Thus, a higher n-value was related to larger h and λ (or lower pre-existing ρ). In the as-deposited multilayers, the pre-existing dislocations would increase with reducing h since the total interface area per unit volume would increase with decreasing h [69]. This is also supported by the evidence that bulk metals (microcrystal Cu) with high dislocation storage capacity for dislocation multiplication and interaction exhibit higher n [1,70], while nanocrystalline metals (Cu) with little dislocation accumulation within grain interiors show lower n [71–74]. The independence of n on ϕ indicates the extrinsic size-independent ρ at fixed h in Fig. 2d. It is suggested that the surface dislocations (which can also act as sources) play a minor role in deformation, since the volume and/or interface source are determined by the characteristic microstructures (e.g. layer thickness and atomic interface structure). One can also see that the multilayers exhibit much higher n than that of Cu at similar intrinsic size in Fig. 2d. Specifically, at $h > 20$ nm, Cu/Zr pillars exhibits relatively higher n, almost equaling that of bulk Cu ($\sim$0.5) [65], while below the transition size $h = 20$ nm, n is quite low, approaching that of ultrafine-nanocrystalline metals ($\sim$0.02–0.2) [61]. This unusual phenomenon implied the transition of dislocation nucleation mechanism similar to that of polycrystalline Cu, i.e. either above or below the transition size $h = 20$ nm, the dislocations can nucleate from different sources such as bulk source or interface source, respectively. In other words, at $h > 20$ nm, dislocations maybe nucleate mainly from the pinned bulk source, while at $h < 10$ nm the interface source is the dominant dislocation source in the Cu/Zr pillars. At the transition size, both the pinned volume and interface sources can product dislocations, in that the dislocation nucleation mechanisms must cross over at some critical size.

4.1.2. Dislocation multiplication and exhaustion

In conventional bulk metals, dislocation multiplication and interaction dominate the ordinary strain hardening (or forest hardening) behavior [1]. Recently, in situ Laue diffraction experiments [75,76] showed that substructures formation can occur at $\varepsilon_p < 5\%$ in 1–10 μm fcc FIBed single crystal pillars, and that strength determined at $\varepsilon_p \geqslant 5\%$ the tenet of "smaller is stronger" is largely due to size-dependent strain hardening (without defining specific individual underlying dislocation mechanisms). This is compatible with the observation that the strength scaling exponent for the size effect increases with the strain at which the stress is derived [77]. Actually, in small-volume materials the number of effective dislocation source and the pre-existing dislocations are sharply reduced, which renders the classical definition of "strain hardening" inappropriate for the ultra-strong nanolayered materials with both high n and θ simultaneously. In such case, ultrahigh strength can be achieved by dislocation exhaustion, i.e. "exhaustion hardening" within the first percent of strain ($\varepsilon_p < 5\%$) [28,76,23], the activated sources being trapped by dislocation reactions.

To sustain the bulk-like behavior (high n and θ) of nanolayered pillars at $h > 20$ nm, there must be lots of dislocation nucleation, multiplication and interaction. A generally accepted model for such multiplication is the F–R (type) source [24,78,79], which can still operate in nanoscaled multilayers [79–81]. Specifically, a regenerative, anomalous dislocation multiplication mechanism resulted from a spontaneous nucleation of partial dislocation loops within the intrinsic stacking fault (ISF; see Fig. 1) achieved in fcc metal by the F–R source [78] ensures that dislocation multiplication is possible, which also renders the more glide–interface dislocation interactions. This not only can induce the high n, also can result in ultrahigh θ. Further reducing h making the F–R (type) source length decreased (even no bulk source), the dislocation nucleation stress is so high that the interface source instead of the bulk source can probably start to switch on. To ensure the dislocations propagate and overcome the resistance from interface dislocations to move forward, cross-slip is a relatively easier way at small length scale, lowering both n and θ simultaneously [67].

4.2. The interrelation between strength and dislocation nucleation

In small-scaled materials, the required stress to generate a dislocation from a source with a length S is proportional to $1/S \ln(S/b)$ [3,12,13,19,30]. The distribution of the nucleation stress is compared to a power law which is used to describe the size effect in tension or compression tests [3,5,12,13]:

$$\sigma \propto C_1 \frac{1}{S} \ln\left(\frac{S}{b}\right) \approx C_2 D^{-m} \quad (6)$$

where C_1 and C_2 are constants, D is the characteristic dimension (e.g. single crystal diameter, grain size and layer thickness) and m is the strength scaling exponent.

4.2.1. Scaling behavior of the strength and activation of dislocation sources

Though no extrinsic size effect was found in compressed $h = 5$ nm nanolayered Cu/Nb micropillars with ϕ spanning from 4 to 8 μm [45], we found from Fig. 3a–f that both the intrinsic characteristic dimensions (h) and the external size limitations (ϕ or β) contribute to the high strength of Cu/Zr micropillars. The strengths $\sigma_{0.2\%}$, $\sigma_{2\%}$ and σ_{max} increase with reducing ϕ or h, which can be described by Eq. (6) with $m = 0.06$–0.45 for ϕ-dependent strength and $m = 0.13$–0.35 for h-dependent strength. Furthermore, m monotonically increases with decreasing h and ϕ (or β). It is suggested that the nanolayered pillars with small intrinsic size exhibit strong size effects. Strikingly, comparing Fig. 3a and c with Fig. 3e, it is found that the ϕ dependence of $\sigma_{0.2\%}$, $\sigma_{2\%}$ and σ_{max} is quite weak at $h > 20$ nm, which can be identified by the low $m = 0.06$–0.10 ($< \sim 0.41$ for Zr pillars and ~ 0.55 for Cu pillars at σ_{max}; see Fig. 3g). This ϕ-insensitive behavior can only be found in bulk metals and pristine single crystals. However, the pre-existing dislocations and the introduction of crystal defects near pillar surfaces can induce markedly size-dependent strength in the present pillars [11,37,82,83]. It thus suggests that dislocations dominantly nucleate from the bulk sources at $h > 20$ nm. The rationale behind this argument is that the characteristic length of FIBed pillars is set by the mean dislocation spacing λ. If the sample intrinsic size is so large that many representative volume elements incorporating all the bulk microstructural characteristics are contained within the sample, conventional size-independent plastic behavior is observed. In addition, the similar m values at different stress levels ($\sigma_{0.2\%}$, $\sigma_{2\%}$ and σ_{max}) further demonstrate the dislocation nucleation is determined by the volume rather than surface/interface sources at this length scale [3,19], because the likelihood of activating a dislocation source (volume or surface/interface sources) at a particular level of stress is up to the statistical distribution in source strengths [37]. On the other hand, the lack of intrinsic size (h) effect on m further demonstrates that the mechanism responsible for the power law itself is insensitive to h, as the h dependence manifests itself as a deviation from the power law, which has been found in the case of $h < 20$ nm (discussed below).

In contrast, a dramatic increase in $m = 0.42$ (~ 4–7 times larger than that of values at large $h > 20$ nm) is observed for $\sigma_{0.2\%}$, $\sigma_{2\%}$ and σ_{max} as h is reduced to 5 nm, respectively (see Fig. 3g). The Cu/Zr pillars corresponding to samples large with respect to a representative volume element show that a size effect could only be derived from operation of surface/interface dislocation sources [37]. In a sense, then, these structures should mimic the yield behavior of defect-free single crystal. The dramatic rise in m indicates that the size-strengthening of FIBed Cu/Zr pillars is much

more pronounced below a transition size $h = 20$ nm, and that the size-dependence itself also has a strong size effect; in other words, the degree of size-strengthening can be very different in distinctly separable h regimes. As the intrinsic size further decreases, the probability that these smaller volumes contain any dislocations is further reduced as well, and eventually dislocation production is predominantly from surface/interface sources.

However, at the median length scale ($h = 10$–20 nm), one can clearly see that m for $\sigma_{0.2\%}$ ($m \sim 0.06$–0.33), $\sigma_{2\%}$ ($m \sim 0.1$–0.28) and σ_{max} ($m \sim 0.15$–0.32) strongly increases with decreasing h, and that m at $h = 10$ nm ($\sigma_{0.2\%} \sim 0.33$, $\sigma_{2\%} \sim 0.28$, $\sigma_{max} \sim 0.32$) is far larger than at $h \geqslant 20$ nm. This indicates an increased size effect as h is reduced, probably, to the order of λ [4,37]. At such length scale, dislocation interactions would not evolve as they do in samples containing many representative volume elements, since mobile dislocations would have a high probability to exit the sample prior to interacting with other dislocations. At this transition size, both the volume and surface/interface sources can switch on. For $h = 20$ nm pillars, at stress level $\sigma_{0.2\%}$, only bulk sources can operate to product dislocation continuously until the source configuration changes (e.g. formation of dislocation multi-junctions exhausting dislocation source) and it can no longer operate at this stress level any more, which renders low $m = 0.06$. Further increasing the stress level (say, $\sigma_{2\%}$), besides that the surface/interface sources begin to switch on (probably heterogeneous dislocation nucleation at stress concentrators), the bulk sources start to operate again and they had shut down just below the corresponding critical stress level to stimulate the sources. At this stress level, we can observe the enhanced size effect. Once again, the sources shut down and are exhausted. The stress level required for the operation of these sources is continually being ratcheted up and eventually the stress level achieves σ_{max} (sufficient increment), which allows for the (almost) simultaneous operation of a new source. In other words, the dislocation nucleation process is analogous to the ratcheting process, i.e. once operating, it never permanently shuts down, but ratchets up (in required stress), including more and more new sources of dislocations as the stress increases. Therefore, at the σ_{max} stress level for $h = 20$ nm pillars, they show a relatively large m (0.15). In contrast, in $h = 10$ nm pillars, the reduced bulk sources and higher nucleation stress causes dislocations mainly nucleate from surface/interface source instead of bulk source, inducing increase in m from ~ 0.15 (at σ_{max} for $h = 20$ nm) to ~ 0.32 (at σ_{max} for $h = 10$ nm).

It should be pointed out that in single crystal pillars (e.g. Au [75] and Ni [77]), transition from exhaustion hardening to ordinary forest hardening can alter values of m. For example, m increases from 0.69 at $\varepsilon_p = 3\%$ to 0.86 at $\varepsilon_p = 10\%$ for Ni pillars [77]. However, in the present study the sharply increased m (from 0.06 to 0.15) with increasing strain (or stress) was only observed in $h = 20$ nm pillars, which indicates a gradual transition from source exhaus-

tion hardening dominated by initiation of sources to bulk strain hardening dominated by dislocation–dislocation interactions as strain increases. It is suggested that below and above the transition size only one dislocation nucleation mechanism dominates the hardening behavior, and also supports the above discussion of dislocation nucleation mechanism transition from bulk source at large h ($m < 0.1$) to surface/interface source at small h ($m > 0.3$).

4.2.2. Intrinsic vs. extrinsic size effect on surface/interface dislocation sources

Another striking feature found in Fig. 3b, d and f, is that m values are close to each other within the scatter for $\sigma_{0.2\%}$, $\sigma_{2\%}$ and σ_{max} at given ϕ or β. Reducing ϕ from 1200 to 300 nm, m monotonically increases from $\sim$0.16 to $\sim$0.35 (see Fig. 3h). The h-dependent strength also suggests that the interfaces must be one of the dislocation sources. The same m at fixed ϕ or β indicates that the stress level needed to activate the source does not vary significantly. However, one can find that as ϕ is reduced down to below 600 nm, m values are almost identical ($m \sim 0.30 \pm 0.03$), which implies the weak ϕ dependence of strength. Due to the dislocation source size and amount scaling with the pillar size or area [22,34,84], the sharp shrinking of ϕ thus can result in a pronounced sample-size-dependent strength at all length scales. However, this is contrary to present results at ϕ = 300–600 nm range. Unlike the surface, the in-plane interface structure (characterized by IBS) of Cu/Zr pillars determined by the constituents' crystal structure is largely h- and ϕ-independent [46,85], which renders the density of interface dislocation source is almost size independent. But the interface source size scales with h [19,68]. Thus, the weak extrinsic dimension effect suggests that the interface is the dominant dislocation source proved by MD simulations [85,86] rather than the surface at such length scale, and that the interface source size is a characteristic of such nanolayered materials, which is less dependent on the sample size.

4.3. Deformation mode map of nanolayered micropillars

The SEM/FIB observations presented above provide clear evidence of a size-dependent deformation behavior, i.e. preferential thinning of Cu at large h and shear localization at small h. This transition stems from dislocation symmetric slip at large h to interface rotation at small h, which has been discussed in detail in our previous results [57]. However, besides the intrinsic size (h), the extrinsic size ϕ (or β) can also influence the deformation behavior of Cu/Zr pillars. The deformation modes for the samples discussed here and from previous publications for nanolayered Cu/Nb [44,45,87] and Al/Pd [56] pillars are summarized in a deformation mode map in Fig. 6 as a function of h and β. Based on the experimental observations, the map can be divided into three regimes: R_I, R_{II} and R_{III}, which are characterized by shear localization, shear + extrusion deformation and extrusion (uniform)
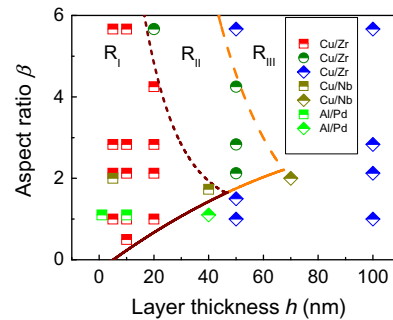

Fig. 6. Deformation mode map for nanolayered pillars. Experimental observations are summarized with data symbols: shear localization (half square) in R_I, shear + extrusion deformation (half circle) in R_{II}, homogeneous uniform extrusion and barreling deformation (half diamond) in R_{III}. Experimental observation results of nanolayered Cu/Nb [44,45,87] and Al/Pd [56] are also included for comparison. The deformation mode map is divided into three regimes described in the text by the lines.

deformation, respectively. In R_I and R_{III}, h is the dominant factor controlling the deformation mode, while in R_{II}, both h and β control the deformation mode.

Interestingly, at very small $h < 50$ nm, the transition from the major shear band with sharp leading fronts to round leading fronts partly supports the tendency of true stress–strain curves (see Fig. 2 for $h = 10$ nm pillars), which show that the large ϕ pillars exhibit strain softening at high strain ($\sim$15%) whereas the small ϕ pillars present softening at relatively low strain ($\sim$10%), indicating the suppression of shear band formation as β is reduced (or ϕ is increased). The larger ϕ is, the higher plastic strain for shear band formation-induced strain softening begins to occur. This suggested that the individual shear banding events are strongly extrinsic size-dependent at such ϕ scale, i.e. in larger pillars the deformation is controlled by nucleation of shear bands, but in smaller pillars it becomes propagation controlled, similar to that of Cu-based amorphous pillars [88]. In other words, as β is increased from 2 to 6 (or higher values), the pillars with small $h < 50$ nm tend to deform homogeneously, i.e. transition from R_I to R_{II} and/or from R_{II} to R_{III}, which is respectively divided by the short dash and dash lines in Fig. 6. At small $\beta < 2$, however, the pillars tend to show homogenous, uniform deformation (at $h > 5$ nm). This manifests that intrinsic size effect itself also possesses strong extrinsic size effect. The underlying physics is that the large ϕ pillar is planar stress state, while the small ϕ pillar is in planar strain state, under compression condition.

Additionally, it should be noted that the transition from uniform to shear deformation observed in rolled Cu/Nb nanolaminates [62] was explained by deformation mechanism transition from dislocation slip in an isolated layer to dislocation cutting cross the interface as well. However, uniaxially tensioned polymer-supported Cu/X (X = Cr, Nb, Zr) multilayers [38,47,48] transformed from opening to shear fracture as shrinking the intrinsic size h. This cannot be simply explained by the deformation mechanism transition mentioned above but can be elucidated by con-

sidering the competition between the *h*-dependent deformability of the ductile Cu layer and intensity of crack initiated in the brittle X layer [38,47,48]. The differences between the compression, rolling and tension test can be ascribed to the different stress states.

5. Conclusions

Systematic compression tests were performed on nano-layered Cu/Zr pillars with a layer thickness ranging from 5 to 100 nm, with pillar diameters varying from 300 to 1200 nm, to examine the intrinsic and extrinsic size effects on the compressive deformation in nanolaminates. The following conclusions can be derived from this study.

1. The paradigm of "smaller is stronger" holds true at a fixed intrinsic or extrinsic size in nanolayered pillars. Competition between the intrinsic and extrinsic size effects results in experimental observation of a transition intrinsic size ∼20 nm, above which the deformation is strongly intrinsic-size-dependent and insensitive to extrinsic size, while below which the two size effects are comparable.
2. At a transition intrinsic size, $h = 20$ nm, the Cu/Zr pillars with extraordinary hardening behavior exhibit the transition from bulk-like behavior to small-volume materials behavior. Below the transition size, dislocations likely nucleate from the interface source of Cu/Zr pillars, above which the dislocations seem to generate from the F–R type bulk source.
3. With shrinking intrinsic size, *h*, the nanolayered pillars show the transition from uniform deformation to local shear band, which is also extrinsic-size-dependent, i.e. in larger pillars the shear banding deformation is controlled by nucleation of shear bands, but in smaller pillars it becomes propagation controlled.

References

[1] Kocks UF, Mecking H. Prog Mater Sci 2003;48:171.
[2] Zhu T, Li J. Prog Mater Sci 2010;55:710.
[3] Dehm G. Prog Mater Sci 2009;54:664.
[4] Arzt E. Acta Mater 1998;46:5611.
[5] Greer JR, De Hosson JTM. Prog Mater Sci 2011;56:654.
[6] Greer JR, Oliver WC, Nix WD. Acta Mater 2005;53:1821.
[7] Uchic MD, Dimiduk DM, Florando JN, Nix WD. Science 2004;305:986.
[8] Volkert CA, Lilleodden ET. Philo Mag 2006;86:5567.
[9] Brinckmann S, Kim J-Y, Greer JR. Phys Rev Lett 2008;100:155502.
[10] Yu Q, Shan Z, Li J, Huang X, Xiao L, Sun J, et al. Nature 2010;463:335.
[11] Jennings AT, Burek MJ, Greer JR. Phys Rev Lett 2010;104:135503.
[12] Uchic MD, Shade PA, Dimiduk DM. Annu Rev Mater Res 2009;39:361.
[13] Kraft O, Gruber PA, Mönig R, Weygand D. Annu Rev Mater Res 2010;40:293.
[14] Ye J, Mishra RK, Sachdev AK, Minor AM. Scripta Mater 2011;64:292.
[15] Sun Q, Guo Q, Yao X, Xiao L, Greer JR, Sun J. Scripta Mater 2011;65:473.
[16] Kim J-Y, Jang D, Greer JR. Acta Mater 2010;58:2355.
[17] Kim J-Y, Jang D, Greer JR. Scripta Mater 2009;61:300.
[18] Schneider AS, Kaufmann D, Clark BG, Frick CP, Gruber PA, Monig R, et al. Phys Rev Lett 2009;103:105501.
[19] Kiener D, Grosinger W, Dehm G, Pippan R. Acta Mater 2008;56:580.
[20] Senger J, Weygand D, Motz C, Gumbsch P, Kraft O. Acta Mater 2011;59:2937.
[21] Shan ZW, Mishra RK, Asif SAS, Warren OL, Minor AM. Nature Mater 2008;7:115.
[22] Greer JR, Nix WD. Phys Rev B 2006;73:245410.
[23] Zhou C, Beyerlein IJ, LeSar R. Acta Mater 2011;59:7673.
[24] Mompiou F, Legros M, Sedlmayr A, Gianola DS, Caillard D, Kraft O. Acta Mater 2012;60:977.
[25] Rao SI, Dimiduka DM, Tang M, Uchic MD, Parthasarathy TA, Woodward C. Philo Mag 2007;87:4777.
[26] Oh SH, Legros M, Kiener D, Dehm G. Nature Mater 2009;8:95.
[27] Tang H, Schwarz KW, Espinosa HD. Phys Rev Lett 2008;100:185503.
[28] Rao SI, Dimiduk DM, Parthasarathy TA, Uchic MD, Tang M, Woodward C. Acta Mater 2008;56:3245.
[29] Kiener D, Minor AM. Acta Mater 2011;59:1328.
[30] Jennings AT, Li J, Greer JR. Acta Mater 2011;59:5627.
[31] Zhu T, Li J, Samanta A, Leach A, Gall K. Phys Rev Lett 2008;100:025502.
[32] Jennings AT, Greer JR. J Mater Res 2011;26:2803.
[33] Huang L, Li QJ, Shan ZW, Li J, Sun J, Ma E. Nature Commun 2011;2:547.
[34] Kiener D, Minor AM. Nano Lett 2011;11:3816.
[35] Greer JR, Weinberger CR, Cai W. Mater Sci Eng A 2008;493:21.
[36] Weinberger CR, Cai W. Proc Nat Acad Sci USA 2008;105:14304.
[37] Rinaldi A, Peralta P, Friesen C, Sieradzki K. Acta Mater 2008;56:511.
[38] Zhang JY, Zhang X, Wang RH, Lei SY, Zhang P, Niu JJ, et al. Acta Mater 2011;59:7368.
[39] Han SM, Phillips MA, Nix WD. Acta Mater 2009;57:4473.
[40] Kim JY, Gu X, Wraith M, Uhl JT, Dahmen KA, Greer JR. Adv Funct Mater 2012. http://dx.doi.org/10.1002/adfm.201103050.
[41] Kim JY, Jang DC, Greer JR. Adv Funct Mater 2011;21:4550.
[42] Phillips MA, Clemens BM, Nix WD. Acta Mater 2003;51:3171.
[43] Bhattacharyya D, Mara NA, Dickerson P, Hoagland RG, Misra A. Acta Mater 2011;59:3804.
[44] Mara NA, Bhattacharyya D, Hirth JP, Dickerson P, Misra A. Appl Phys Lett 2010;97:021909.
[45] Mara NA, Bhattacharyya D, Dickerson P, Hoagland RG, Misra A. Appl Phys Lett 2008;92:231901.
[46] Misra A, Hirth JP, Hoagland RG. Acta Mater 2005;53:4817.
[47] Zhang JY, Zhang X, Liu G, Zhang GJ, Sun J. Mater Sci Eng A 2011;528:2982.
[48] Zhang JY, Zhang X, Liu G, Zhang GJ, Sun J. Scripta Mater 2010;63:101.

[49] Liu Y, Bufford D, Wang H, Sun C, Zhang X. Acta Mater 2011;59:1924.
[50] Anderson PM, Li C. Nanostruct Mater 1995;5:349.
[51] Misra A, Hirth JP, Kung H. Philos Mag A 2002;82:2935.
[52] Phillips MA, Clemens BM, Nix WD. Acta Mater 2003;51:3157.
[53] Rao SI, Hazzledine PM. Philos Mag A 2000;80:2011.
[54] Hoagland RG, Kurtz RJ, Henager CH. Scripta Mater 2004;50:775.
[55] Singh DRP, Chawla N, Tang G, Shen YL. Acta Mater 2010;58:6628.
[56] Dayal P, Quadir MZ, Kong C, Savvides N, Hoffman M. Thin Solid Films 2011;519:3213.
[57] Zhang JY, Lei SY, Liu Y, Niu JJ, Chen Y, Liu G, et al. Acta Mater 2012;60:1610.
[58] Lei SY, Zhang JY, Niu JJ, Liu G, Zhang X, Sun J. Scripta Mater 2012;66:706.
[59] Sneddon IN. Int J Eng Sci 1965;3:47.
[60] Lee S-W, Han SM, Nix WD. Acta Mater 2009;57:4404.
[61] Lu L, Chen X, Huang X, Lu K. Science 2009;323:607.
[62] Misra A, Hoagland RG. J Mater Sci 2006;42:1765.
[63] Bouaziz O, Estrin Y, Bréchet Y, Embury JD. Scripta Mater 2010;63:477.
[64] Sinclair CW, Poole WJ, Bréchet Y. Scripta Mater 2006;55:739.
[65] Chaudhri MM. Acta Mater 1998;46:3047.
[66] Ebrahimi R, Pardis N. Mater Sci Eng A 2009;518:56.
[67] Misra A, Zhang X, Hammon D, Hoagland RG. Acta Mater 2005;53:221.
[68] Gruber PA, Böhm J, Onuseit F, Wanner A, Spolenak R, Arzt E. Acta Mater 2008;56:2318.
[69] Csiszár G, Misrab A, Ungár T. Mater Sci Eng A 2011;528:6887.
[70] Nes E. Prog Mater Sci 1997;41:129.
[71] Kumar KS, Van Swygenhoven H, Suresh S. Acta Mater 2003;51:5743.
[72] Dao M, Lu L, Asaro RJ, De Hosson JTM, Ma E. Acta Mater 2007;55:4041.
[73] Zhang JY, Liu G, Wang RH, Li J, Sun J, Ma E. Phys Rev B 2010;81:172104.
[74] Zhang JY, Zhang X, Liu G, Wang RH, Zhang GJ, Sun J. Mater Sci Eng A 2011;528:7774.
[75] Maaß R, Van Petegem S, Ma D, Zimmermann J, Grolimund D, Roters F, et al. Acta Mater 2009;57:5996.
[76] Maaß R, Uchic MD. Acta Mater 2012;60:1027.
[77] Frick CP, Clark BG, Orso S, Schneider AS, Arzt E. Mater Sci Eng A 2008;489:319.
[78] Koning Md, Cai W, Bulatov VV. Phys Rev Lett 2003;91:025503.
[79] Beanland R. J Appl Phys 1992;72:4031.
[80] Matthews JW, Blakeslee AE. J Crystal Growth 1974;27:118.
[81] Cherns D, Stowell MJ. Thin Solid Films 1975;29:107.
[82] Kiener D, Motz C, Rester M, Jenko M, Dehm G. Mater Sci Eng A 2007;459:262.
[83] Mayer J, Giannuzzi LA, Kamino T, Michael J. MRS Bull 2007;32:400.
[84] Ng KS, Ngan AHW. Scripta Mater 2008;59:796.
[85] Wang J, Misra A. Curr Opin Solid State Mater Sci 2011;15:20.
[86] Zhang RF, Wang J, Beyerlein IJ, Germann TC. Scripta Mater 2011;65:1022.
[87] Li N, Mara NA, Wang YQ, Nastasi M, Misra A. Scripta Mater 2011;64:974.
[88] Chen CQ, Pei YT, De Hosson JTM. Acta Mater 2010;58:189.